



Article

Optical Force of Bessel Pincer Light-Sheets Beam on a Dielectric Sphere of Arbitrary Size

Shu Zhang *, Bing Wei, Qun Wei, Renxian Li , Shiguo Chen and Ningning Song

School of Physics, Xidian University, Xi'an 710071, China

* Correspondence: zhangs@stu.xidian.edu.cn

Abstract: In the framework of Generalized Lorenz–Mie theory (GLMT), based on the expansion results of electromagnetic field radiation components of Bessel pincer light sheets beam acting on dielectric particles of arbitrary size, the expression of radiation force components in a Cartesian coordinate system is obtained by using the Maxwell stress tensor method. On the one hand, the effects of the refractive index and the equivalent radius of spherical particles on the distribution of radiation force are discussed; On the other hand, the influence of beam scaling parameter and beam order of Bessel pincer light sheets beam on the distribution of radiation force are investigated. The results indicate that the changes of particle's refractive index and effective radius only affect the distribution of radiation force. However, the beam scaling parameter and beam order of Bessel pincer light sheets beam have a very sharp impact on the convergence position, distribution range and bending degree far away from the wave source of the radiation force. Single-beam optical tweezers using the self-focusing and self-bending Bessel pincer light-sheets beam are crucial for applications such as single molecule biophysics, optical manipulation and particle separation/clearing.

Keywords: Bessel pincer light-sheets; GLMT; optical force; Maxwell's stress tensor; angular spectrum expansion method



Citation: Zhang, S.; Wei, B.; Li, R.; Wei, Q.; Chen, S.; Song, N. Optical Force of Bessel Pincer Light-Sheets Beam on a Dielectric Sphere of Arbitrary Size. *Nanomaterials* **2022**, *12*, 3723. <https://doi.org/10.3390/nano12213723>

Academic Editor: Antonio Di Bartolomeo

Received: 29 September 2022

Accepted: 19 October 2022

Published: 23 October 2022

Publisher's Note: MDPI stays neutral with regard to jurisdictional claims in published maps and institutional affiliations.



Copyright: © 2022 by the authors. Licensee MDPI, Basel, Switzerland. This article is an open access article distributed under the terms and conditions of the Creative Commons Attribution (CC BY) license (<https://creativecommons.org/licenses/by/4.0/>).

1. Introduction

The optical scattering, extinction and absorption cross section characterize the strength of light-matter interaction. They quantify the fraction of power a particle scatters, extincts, or absorbs. Although the optical force is another one to characterize the interaction between target and electromagnetic wave. Optical forces stem from momentum transfer directly between photons and objects, or indirectly between surrounding media and objects when light interacts with objects. Optical trapping [1] (due to strongly focused beam on the object), optical pulling [2] (due to scattering force) and optical binding [3] (Multiple scattering between particles) are there typical beam types. We are interested in the type of optical trapping for a monochromatic beam—optical tweezer. Optical tweezers are exquisite position and force transducers. Therefore, they are widely used for high-resolution measurements in fields as varied as physics [4,5], biology [6–9], optical lift [10,11], all-optical wavelength routing [12], optical scalpels and scissors [13–15], optical stochastic cooling [16,17], optical force sensor [18], Dynamic-Microscopy [19], and materials science [20]. The forces exerted by carefully sculpted wavefronts of light [21] offer precisely the level of access and control needed for rapid progress across all of these fields.

Since the discovery that a comet's tail points away from the sun, theoretically explained by Maxwell (1883) [22], experimentally proved by Lebedev [23] and Nichols and Hull [24], light processes have been known to exert optical radiation pressure. The optical tweezer [25,26], first proposed by Arthur Ashkin and coworkers at AT&T Bell Laboratories, has been a classical tool for optical manipulating and trapping of micrometer-sized particles. Particle characteristics and light source characteristics of optical tweezers are

the key factors in the operation of optical tweezers. The techniques used for manipulating microparticles rely on the electric dipole interaction energy [27,28], which scales down approximately with particle volume. Thus, thermal fluctuations are large enough to overwhelm the trapping forces at the nanoscale [29]. The method of discrete dipole approximation [30–32] is the typical one to manipulate particles using the dipole model. However, it is limited to the particle size, whose size is close to the wavelength ($|mkd| < 1$, m is the refractive index, k is the wave number and d is the distance of dipole). Mie–Debye theory [33], is applicable to these large particles (larger than the wavelength). The Rayleigh method [34] is a universal one to those small particles (smaller than the wavelength). The above method is confined to electromagnetic calculation of a single size (compared to wavelength). Theoretical expressions for the internal and external electromagnetic fields of a homogeneous spherical particle illuminated by a focused laser beam based upon a rigorous, complete solution of Maxwell's equations have been developed, each utilizing different approaches, by Kim and Lee [35] Gouesbet, Maheu, and Grehan [36] and Barton, Alexander, and Schaub [37]. They can be used to calculate optical force on the particles of arbitrary size. Bardon et al. [38] derived series expressions for net radiation force and net torque for a spherical particle by an arbitrary defined monochromatic beam. This provides a common method for the optical force calculating using the Maxwell stress tensor [39,40], under the steady-state condition. The optical force depends not only on the property of the target itself but also on the configuration of the incident beam [41]. Light waves carry energy and momentum. If light is scattered or absorbed by a particle, its momentum is changed, and by conservation of momentum, it exerts a force on the particle called radiation pressure.

To illustrate the trapping of optical force, it is significant to describe the wavefront modification of the incident beam. A Gaussian beam [42] is one of the classical and early optical tweezers' sources. The focusing characteristics of a Gaussian beam have universal applications [32,43] in optical manipulation. However, it is easily limited by diffraction in long-distance scattering. Bessel beams [44–49] with self-reconstruction and non-diffraction characteristics break through the distance limit. Airy beams [50,51], with the properties of the acceleration transverse and non-diffraction, supports the bending angles along the propagation direction, and thus the Airy beam is convenient for particle clearing [52], optical force switching [53] and Optical Force-Fluorescence [41]. Recently, the two-dimensional illustration of living tissue is one of important researches to reveal the characteristics of biological tissue, such as in optofluidics [54] involving particle surface analyses, and light-based imaging modalities [55] in biomedicine to the refinement and technical improvement of light-sheet imaging. Mitri has done many works in light-beams in Airy light-sheets [56,57], Bessel–Gaussian light-sheets [58], fractional Bessel–Gauss pincers light-sheets [59], using the methods of analytical method and discrete dipole approximation (DDA). However, the bending angle of Airy beam is relatively small. The larger bending angles and auto-focusing are needed in some situations, such as in particle manipulation applications with minimal hampering by obstacles. The Bessel pincer, first proposed by Mitri, exhibits a negative force by a higher-order Bessel beam in the context of acoustical/scalar waves. Bessel pincer light-sheet beams [60] provide enhanced auto-focusing and curving/bending capabilities. In our method [61], the slice-section with a 'thin sheet' of Bessel pincer light-sheets beam is considered. Dielectric materials [62,63] are widely used in target electromagnetic scattering [64,65] because of their dielectric properties [66,67] under an electric field.

According to the given components of the incident electric field and scattering field in ref. [61], the Maxwell stress tensor is obtained. Subsequently, the net force on the particle can be determined by integrating the dot product of the outwardly directed normal unit vector and Maxwell stress tensor over a surface enclosing the particle. The influences of the Bessel pincer light-sheets (mainly focusing on beam order and scaling parameter) acting on a dielectric sphere particle (mainly focusing on the refractive index and dimensionless particle size), will be discussed.

2. Methods

2.1. Angular of Bessel Pincer Light-Sheets Beam

Considering the TE polarization of Bessel pincer light-sheets beam, the angular spectrum of Bessel pincer [60] is as below:

$$\begin{aligned}
 S_x(p, q) &= \left(\frac{kE_0}{2\pi}\right) \int_{-\infty}^{+\infty} J_l(\alpha ky) e^{-ikpy} dy \\
 &= \frac{E_0 i^{-l}}{k\alpha_0^l \sqrt{\alpha_0^2 - p^2}} \Re \left\{ \left(p + i\sqrt{\alpha_0^2 - p^2} \right)^l \right\}
 \end{aligned}
 \tag{1}$$

where, α_0 is the beam scaling parameter; l is the beam order; (p, q) is the directional cosines ($p = \sin \alpha$ and $q = \cos \alpha$), and α is the angle of propagation of the individual plane wave. Assuming the dielectric sphere is illuminated by the Bessel pincer light-sheets beam, as shown in Figure 1, and the the location of the wave source is at $(y_0, z_0) = (0, 0)$. Through the multipole expansion of the incident plane wave and considering the orthogonal property of vector spherical wave function, the series expression of incident plane wave is obtained.

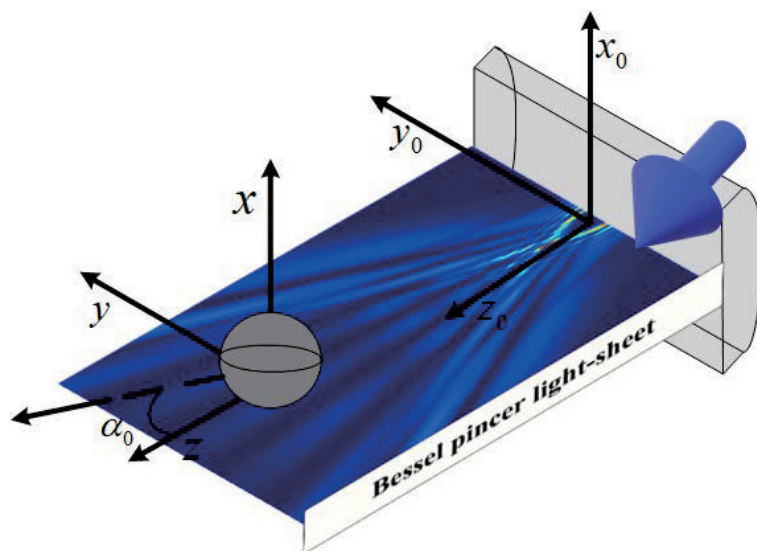


Figure 1. Distribution of radiation force component F_z under the illumination of Bessel pincer light-sheets beam ($\lambda = 0.6328 \mu\text{m}$, $\alpha_0 = 0.5$ and $l = 10$) on the dielectric sphere (radius is $0.1 \mu\text{m}$).

$$\mathbf{E}_i = - \sum_{n=1}^{\infty} \sum_{m=-n}^n iE_{mn} \left[p_{mn} \mathbf{N}_{mn}^{(1)}(k\mathbf{r}) + q_{mn} \mathbf{M}_{mn}^{(1)}(k\mathbf{r}) \right]
 \tag{2}$$

where,

$$E_{mn} = i^n |E_0| \left[\frac{2n+1}{n(n+1)} \frac{(n-m)!}{(n+m)!} \right]^{1/2}
 \tag{3}$$

$$\mathbf{M}_{mn}^{(1)}(k\mathbf{r}) = [i\pi_{mn}(\cos \theta) \mathbf{e}_\theta - \tau_{mn}(\cos \theta) \mathbf{e}_\phi] j_n(kr) e^{im\phi}
 \tag{4}$$

$$\begin{aligned}
 \mathbf{N}_{mn}^{(1)}(k\mathbf{r}) &= [\tau_{mn}(\cos \theta) \mathbf{e}_\theta + i\pi_{mn}(\cos \theta) \mathbf{e}_\phi] \frac{1}{kr} \frac{d}{dr} [r j_n(kr)] e^{im\phi} \\
 &+ \mathbf{e}_r n(n+1) P_n^m(\cos \theta) \frac{j_n(kr)}{kr} e^{im\phi}
 \end{aligned}
 \tag{5}$$

with

$$p_{mn} = k \frac{i^{1-m}}{E_0} D_{mn}^{1/2} \int_{\alpha=0}^{\pi/2} d\alpha e^{-ik \cos \alpha z_0} S_x(\alpha) \pi_{mn}(\cos \alpha) \cos \alpha
 \tag{6}$$

$$q_{mn} = k \frac{i^{1-m}}{E_0} D_{mn}^{1/2} \int_{\alpha=0}^{\pi/2} d\alpha e^{-ik \cos \alpha z_0} S_x(\alpha) \tau_{mn}(\cos \alpha) \cos \alpha \tag{7}$$

$$D_{mn} = \frac{(2n+1)(n-m)!}{n(n+1)(n+m)!} \tag{8}$$

$$\pi_{mn}(\cos \theta) = \frac{m}{\sin \theta} P_n^m(\cos \theta) \tag{9}$$

$$\tau_{mn}(\cos \theta) = \frac{dP_n^m(\cos \theta)}{d\theta} \tag{10}$$

where $P_n^m(\cos \alpha)$ represents the associated Legendre polynomials of degree n and order m , $j_l(\cdot)$ is the spherical Bessel function of l order, and $\mathbf{e}_{(r,\theta,\phi)}$ are radial, polar and azimuthal unit vectors, respectively.

2.2. Optical Force on a Sphere

Following the previous work, we broaden the scattering of a Bessel pincer light-sheets beam to optical force. The net radiation force can be determined by integrating the dot product of the outwardly directed normal unit vector $\hat{\mathbf{r}}$ and Maxwell's stress tensor [35,68] over a surface enclosing the particle.

$$\mathbf{F} = \oint_S \hat{\mathbf{r}} \cdot \langle \overset{\leftrightarrow}{\mathbf{T}} \rangle dS \tag{11}$$

where, S is arbitrary closed surface surrounding the particle, and $\hat{\mathbf{r}}$ is the unit normal vector at arbitrary point on the surface. $\overset{\leftrightarrow}{\mathbf{T}}$ is the Maxwell stress tensor, written as

$$\langle \overset{\leftrightarrow}{\mathbf{T}} \rangle = \frac{1}{2} \text{Re} \left[\epsilon \mathbf{E} \mathbf{E}^* + \mu \mathbf{H} \mathbf{H}^* - \frac{1}{2} (\epsilon \mathbf{E} \cdot \mathbf{E}^* + \mu \mathbf{H} \cdot \mathbf{H}^*) \overset{\leftrightarrow}{\mathbf{I}} \right] \tag{12}$$

where, $\overset{\leftrightarrow}{\mathbf{I}}$ is the unit tensor, and ϵ and μ are the permittivity and permeability coefficient of particles, respectively. For the loss-free environment and unbounded closed surface, the Cartesian component of the optical force acting on a spherical particle is below,

$$F_x = \text{Re}[F_1], \quad F_y = \text{Im}[F_1], \quad F_z = \text{Re}[F_2] \tag{13}$$

where,

$$F_1 = \frac{2\pi\epsilon_0}{k^2} |E_0|^2 \sum_{n=1}^{\infty} \sum_{m=-n}^n \left\{ \begin{aligned} & \left[\frac{[(n-m)(n+m+1)]^{\frac{1}{2}}}{n(n+1)} \right. \\ & \times \left(\begin{aligned} & \tilde{a}_{m,n} \tilde{b}_{m+1,n}^* + \tilde{b}_{m,n} \tilde{a}_{m+1,n}^* \\ & - \tilde{p}_{m,n} \tilde{q}_{m+1,n}^* - \tilde{q}_{m,n} \tilde{p}_{m+1,n}^* \end{aligned} \right) \\ & - \left[\frac{n(n+2)(n+m+1)(n+m+2)}{(n+1)^2(2n+1)(2n+3)} \right]^{\frac{1}{2}} \times \left(\begin{aligned} & \tilde{a}_{m,n} \tilde{a}_{m+1,n+1}^* + \tilde{b}_{m,n} \tilde{b}_{m+1,n+1}^* \\ & - \tilde{p}_{m,n} \tilde{p}_{m+1,n+1}^* - \tilde{q}_{m,n} \tilde{q}_{m+1,n+1}^* \end{aligned} \right) \\ & + \left[\frac{n(n+2)(n-m)(n-m+1)}{(n+1)^2(2n+1)(2n+3)} \right]^{\frac{1}{2}} \times \left(\begin{aligned} & \tilde{a}_{m,n+1} \tilde{a}_{m+1,n}^* + \tilde{b}_{m,n+1} \tilde{b}_{m+1,n}^* \\ & - \tilde{p}_{m,n+1} \tilde{p}_{m+1,n}^* - \tilde{q}_{m,n+1} \tilde{q}_{m+1,n}^* \end{aligned} \right) \end{aligned} \right\} \tag{14}$$

and

$$F_2 = -\frac{4\pi\epsilon_0}{k^2} |E_0|^2 \sum_{n=1}^{\infty} \sum_{m=-n}^n \left\{ \frac{m}{n(n+1)} \times (\tilde{a}_{m,n} \tilde{b}_{m,n}^* - \tilde{p}_{m,n} \tilde{q}_{m,n}^*) + \left[\frac{n(n+2)(n-m+1)(n+m+1)}{(n+1)^2(2n+1)(2n+3)} \right]^{\frac{1}{2}} \times \left(\begin{aligned} & \tilde{a}_{m,n} \tilde{a}_{m,n+1}^* + \tilde{b}_{m,n} \tilde{b}_{m,n+1}^* \\ & - \tilde{p}_{m,n} \tilde{p}_{m,n+1}^* - \tilde{q}_{m,n} \tilde{q}_{m,n+1}^* \end{aligned} \right) \right\} \tag{15}$$

with

$$\begin{aligned}\tilde{a}_{m,n} &= a_{m,n} - \frac{1}{2}p_{m,n}, & \tilde{p}_{m,n} &= \frac{1}{2}p_{m,n} \\ \tilde{b}_{m,n} &= b_{m,n} - \frac{1}{2}q_{m,n}, & \tilde{q}_{m,n} &= \frac{1}{2}q_{m,n}\end{aligned}\quad (16)$$

a_n and b_n are the classical Mie coefficients [33]. Since the energy of the incident light is proportional to $|E_0|^2$ in Equation (11), the formula states that the net radiation force on the particle is proportional to the energy of the incident beam [35].

3. Results

This section mainly includes three parts: Firstly, compare and verify the simulation results under different numerical methods; Secondly, the influence of particle parameters (refractive index of sphere, particle radius) and beam parameters (beam scaling parameters α_0 and beam order l) on the force spatial distribution is analyzed; Thirdly, the trend of particle parameters (refractive index of sphere, particle radius) and beam parameters (beam scaling parameters α_0 and beam order l) with beam propagation position is discussed.

3.1. Numerical Validation

In this part, the simulation results based on different numerical methods are given. Initialization parameters are as follows: the incident wavelength of Bessel pincer light-sheets beam is 1.064 μm ; the refractive index of the sphere is 1.59 and the ambient refractive index is 1.33; the radius of sphere is 0.01 μm ; the scaling parameter α_0 is equal to 0.1 and the beam order l is 1.

3.1.1. Incident Intensity

With all above parameters pre-determined, Figure 2 shows the change trend of the incident field intensity of Bessel pincer with the spatial position under two polarization modes (TE and TM), using analytical method (JXJ-blue curve plus Pentagram) (method in [60]) and reconstruction method (yellow curve plus Pentagram—the method used in this paper). With the change of the spatial distance y , the field intensity distribution trends of the incident field (corresponding to the two methods) have good consistency. Two numerical methods are used to supplement the verification of paper [59], which shows the effectiveness of the reconstruction method.

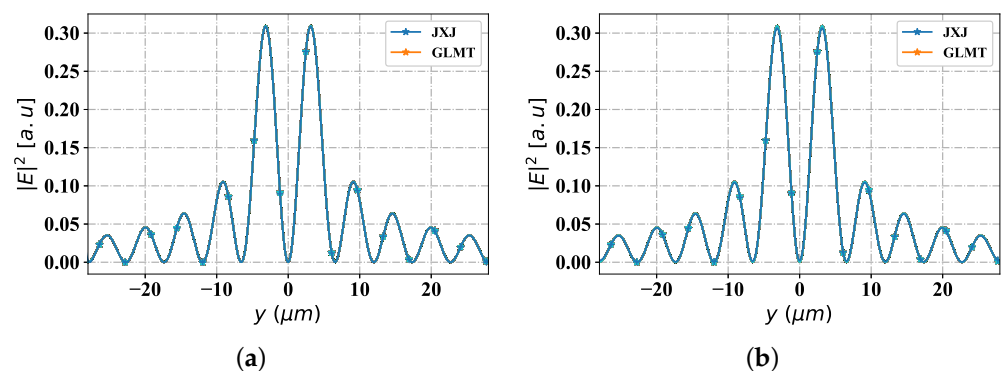


Figure 2. Validation of different $|E|^2$ with GLMT, and JXJ. (a) TE; (b) TM.

3.1.2. Force Component of f_y and f_z

Furthermore, to clearly demonstrate the availability of optical force, the feasibility of the radiation force results is verified by comparing the calculation results of radiation force components of the Rayleigh method [44] and the Maxwell stress tensor method based on GLMT reconstruction. As shown in Figure 3a, it can be deduced from the line profile that the force component F_y is in good agreement with both Rayleigh and GLMT (Maxwell stress tensor). The same is true of the force component F_z (Figure 3b)—there is good consistency of the two methods.

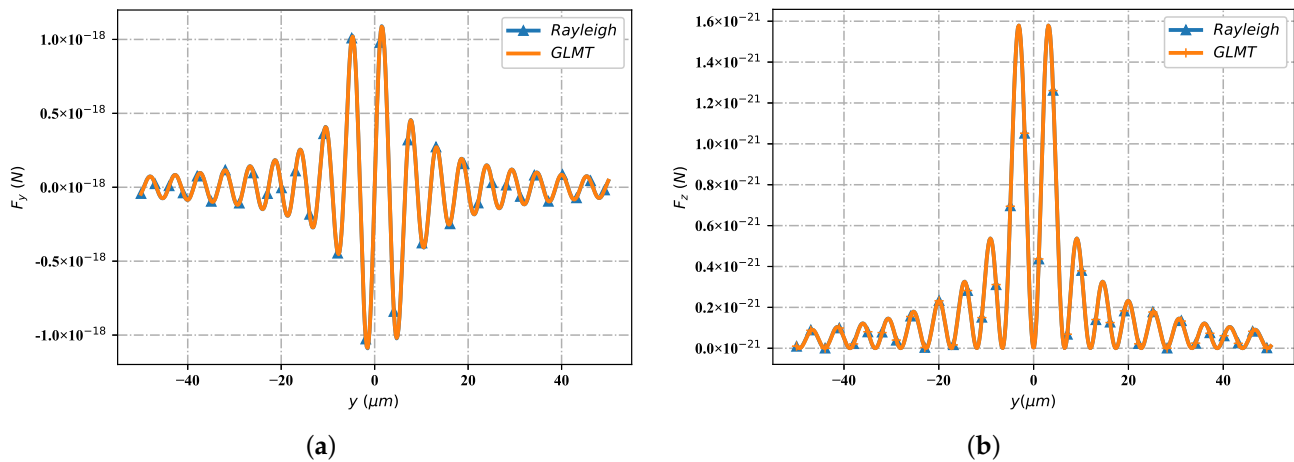


Figure 3. Validation of different F_y and F_z with Rayleigh and GLMT. (a) F_y ; (b) F_z .

3.2. Longitudinal and Transverse Optical Force F_y and F_z

This part gives the radiation force components F_y and F_z in the yz plane with the change of spatial position, with emphasis on the influence of particle refractive index, particle equivalent radius (relative to wavelength), beam scaling parameter α_0 and beam order l . Assuming that the amplitude of the electric field is equal to $E_0 = 1.0 \times 10^6$ V/m. The refractive index of environmental medium is defined as $m_2 = 1.36$ (ethylalcohol environment), and that of particle is $m_1 = 1.5$. The wavelength of incident Bessel pincer light-sheets beam is set to $\lambda = 0.532$ μm .

3.2.1. Different Radius of the Particle

Here, the spatial distribution of radiation force component F_y with the change of particle equivalent radius, is illustrated in Figure 4. The beam scaling parameter α_0 is 0.5 and beam order l is 10. The radius of spherical particle is defined as 0.001λ , 0.01λ , 0.1λ and 1λ , respectively. Figure 4a displays the distribution of optical force component F_y , shows the moderate distribution range along the y -axis, the beam convergence point close to the wave source, and the bending angle with a certain expansion angle along the z -axis, far from the convergence point. Equally, Figure 4b shows the range of distribution along the y -axis with the same width as that in Figure 4a, the beam convergence point at the same location as in Figure 4a, and the bending angle with the same bending degree away from the convergence point as in Figure 4a. The distribution in Figure 4c,d is the same as that in Figure 4a. In particular, the values of the optical force component F_y vary greatly. Specifically, the order of magnitude of F_y in Figure 4a is smaller than that of the third power of 10 in Figure 4b, the fifth power of 10 in Figure 4c and the eighth power of 10 in Figure 4d.

Figure 5 shows the longitudinal optical force component F_z with spherical particles of different radius sizes. The simulation parameters are consistent with Figure 4. From Panel (a) to (d), the F_z distribution range along y -axis, has the identical distribution range and location. The position of beam convergence point shall be consistent, and the bending degree of the beam away from the beam convergence point is almost the same. Similar to the distribution of optical component F_y under different particle sizes, the magnitude of the F_z value is the difference of optical force component F_z distribution under different particle sizes. Moreover, the larger the particle radius is, the higher the corresponding F_z value is.

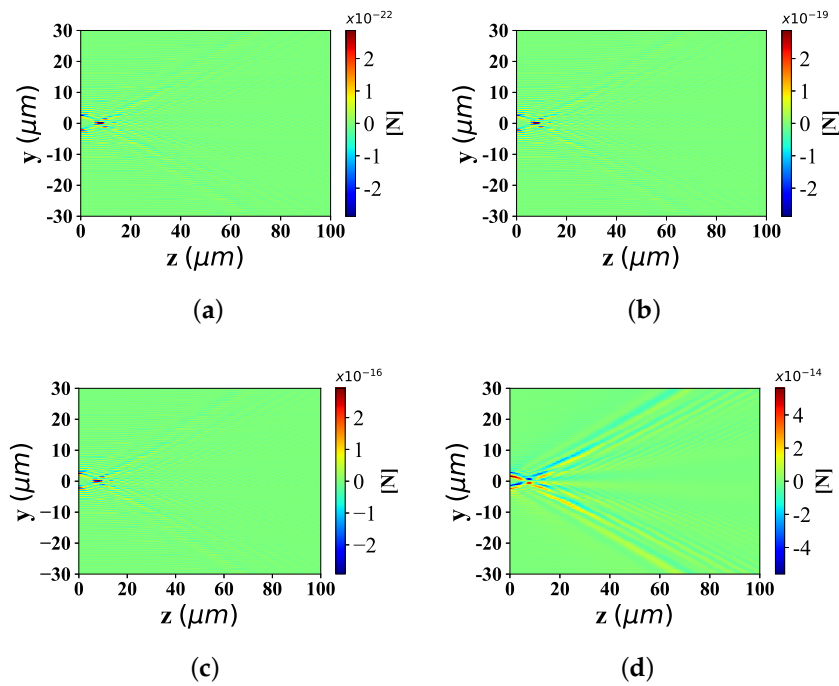


Figure 4. Distribution of F_y under different spherical radius (radius is equal to 0.001λ , 0.01λ , 0.1λ and λ , respectively) acting on Bessel pincer light-sheets beam ($\lambda = 0.532 \mu\text{m}$, $\alpha_0 = 0.5$, and $l = 10$). (a) radius = 0.001λ ; (b) radius = 0.01λ ; (c) radius = 0.1λ ; (d) radius = 1λ .

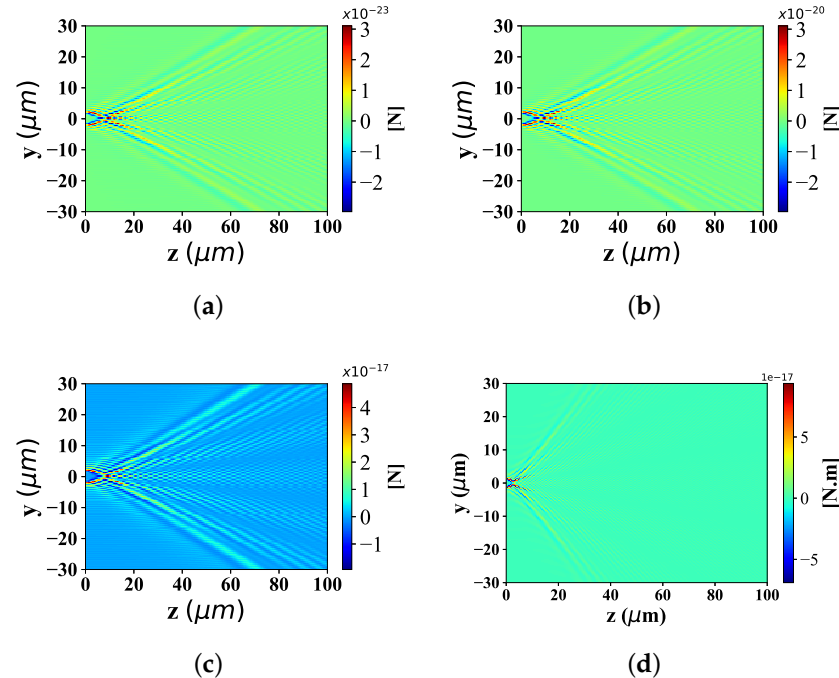


Figure 5. Distribution of F_z under different spherical radius (radius is set to 0.001λ , 0.01λ , 0.1λ and λ) acting on Bessel pincer light-sheets beam ($\lambda = 0.532 \mu\text{m}$, $\alpha_0 = 0.5$, and $l = 10$). (a) radius = 0.001λ ; (b) radius = 0.01λ ; (c) radius = 0.1λ ; (d) radius = 1λ .

3.2.2. Different Beam Scaling Parameter α_0 of Bessel Pincer Light-Sheets Beam

Here are the noticeable trends of the optical force component F_y and F_z in the $y - z$ plane, with different beam scaling parameter α_0 ($\alpha_0 = 0.2, 0.5, 0.8$). The beam order is $l = 10$ and the spherical radius is set to $0.1 \mu\text{m}$.

As can be seen in Figure 6, the distributions about optical force component F_y are illustrated with different beam scaling parameters. From the point of the trend of distribution range along the y -axis, Figure 6a has a fairly wide distribution range. There is a small distribution range in Figure 6b, which is much smaller than that in Figure 6a. Figure 6c retains some of the distribution range, but has the smallest distribution range among the three. From the perspective of beam convergence point position along z -axis, in Figure 6a, the distance between the convergence point of Bessel pincer light sheets beam and the source point of the wave source is dozens of wavelengths. In Figure 6b, the assembly position of the Bessel pincer light sheets beam is much closer to the wave source than that in Figure 6a. In contrast, the source position of Bessel pincer light sheets beam in Figure 6c is closer to the wave source than that in Figure 6b.

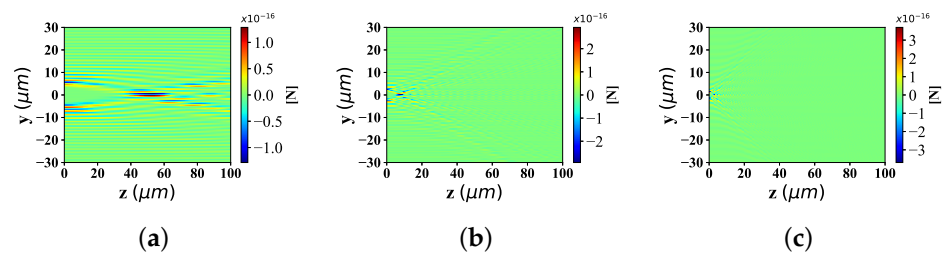


Figure 6. Distribution of F_y under the interaction between the sphere and Bessel pincer light-sheets beam with different beam scaling parameter α_0 ($\alpha_0 = 0.2, 0.5,$ and 0.8 ; beam order is $l = 10$). (a) $\alpha_0 = 0.2$; (b) $\alpha_0 = 0.5$; (c) $\alpha_0 = 0.8$.

In Figure 7, the distribution of optical force component F_z with different beam scaling parameter α_0 can be seen. Similar to the perspective analysis in Figure 6, the distribution range of the optical component F_z along the z -axis in Figure 7a, is the longest range, followed by Figure 7b,c which is the shortest of the three. Considering the distance between the convergence point of Bessel pincer light sheets beam and the wave source, the location of the beam convergence point in Figure 7a is the farthest from the wave source, followed by Figure 7b, and Figure 7a which is the closest among the three.

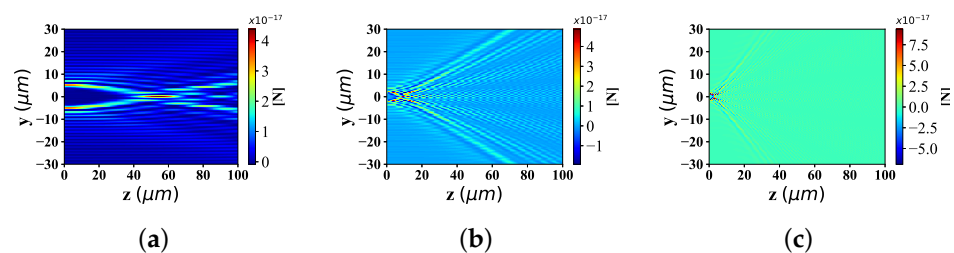


Figure 7. Distribution of F_z under the interaction between the sphere and Bessel pincer light-sheets beam with different beam scaling parameter α_0 ($\alpha_0 = 0.2, 0.5,$ and 0.8 ; beam order is $l = 10$). (a) $\alpha_0 = 0.2$; (b) $\alpha_0 = 0.5$; (c) $\alpha_0 = 0.8$.

3.2.3. Different Beam Order l of Bessel Pincer Light-Sheets Beam

According to the Figures 8 and 9, the changing trend of optical radiation force component F_y and F_z in yz space position (particle radius is 0.1λ , beam scale parameter is $\alpha_0 = 0.5$) with the change of beam order (even order is 6, 12, 26, and odd order is 5, 45, 85), is discussed.

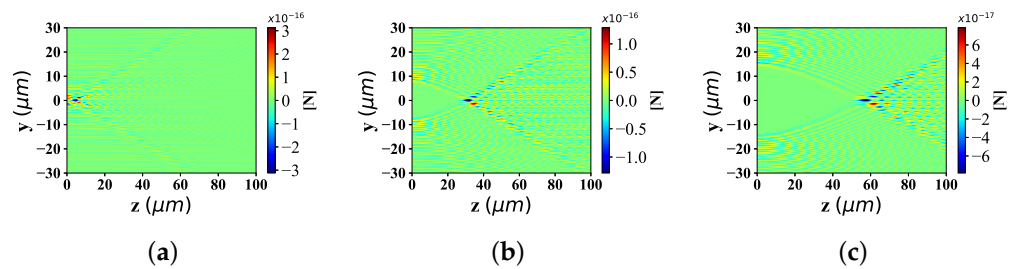


Figure 8. Distribution of F_y under the interaction between the sphere and Bessel pincer light-sheets beam with different beam order l ($l = 5, 45, 85$; $\alpha_0 = 0.5$; radius is $0.1 \mu\text{m}$). (a) $t = 5$; (b) $t = 45$; (c) $t = 85$.

Figure 8a–c give the distribution of radiation force component F_y under different beam orders when the beam order l is odd. The distribution range of the radiation force component F_y along the y -axis in Figure 8b is much wider than that in Figure 8a, and the location of the beam convergence point is farther from the location of the wave source than that in Figure 8a. Moreover, the bending degree of the beam far from the beam convergence point in Figure 8b is larger than the angle in Figure 8a. Further, when the radial force component F_y is distributed along the y -axis, Figure 8c has a much wider range than that in Figure 8b; The position of the beam convergence point is farther than that in Figure 8b, and the scattering angle of the beam far away from the convergence point is more curved than that in Figure 8b.

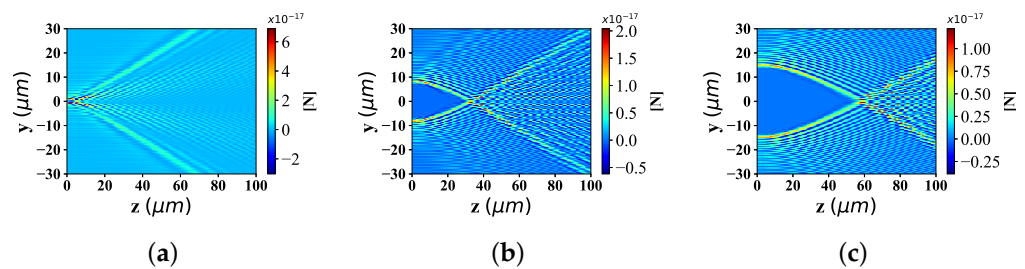


Figure 9. Distribution of F_z under the interaction between the sphere and Bessel pincer light-sheets beam with different beam order l ($l = 5, 45, 85$; $\alpha_0 = 0.5$; radius is $0.1 \mu\text{m}$). (a) $t = 5$; (b) $t = 45$; (c) $t = 85$.

The distribution of radiation force component F_z under different beam orders, is discussed in Figure 9. Similar to the distribution of F_y values in Figure 8, the variation range of F_z number along the y -axis increases with the growing of beam order; The beam convergence point position of F_z value ascends with the raising of the beam order l ; However, the spreading degree of the Bessel pincer light-sheets beam (far from the convergence point), decreases with the increase of the beam order.

3.2.4. Different Refractive Indices of the Particle

The particle refractive index affects the absorption of beam particle interaction. The distribution of optical radiation force component F_y and F_z under the influence of particle refractive index, is shown in Figures 10 and 11, including the part higher than the environmental refractive index ($m_1 = 1.8, 2.8$ and 3.8 , respectively) and the part lower than the environmental refractive index ($m_1 = 1.0, 1.2$, and 1.3 , respectively). The beam scaling parameter is $\alpha_0 = 0.5$, the beam order is $l = 10$, and the particle radius is $0.1 \mu\text{m}$.

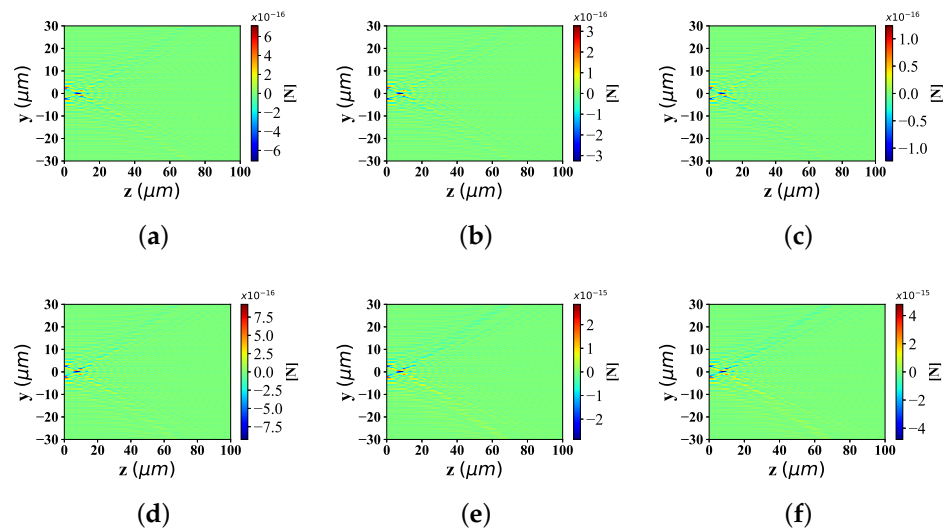


Figure 10. Distribution of F_y under different refractive indices ($m_1 = 1.0, 1.2, 1.3, 1.8, 2.8, 3.8$) for the interaction of Bessel pincer light-sheets beam on the spherical particle. (a) $m_1 = 1.0$; (b) $m_1 = 1.2$; (c) $m_1 = 1.3$; (d) $m_1 = 1.8$; (e) $m_1 = 2.8$; (f) $m_1 = 3.8$.

Figure 10 depicts the distributions of optical force component F_y under different refractive indices of the particle. For the case where the particle refractive index is less than the environmental refractive index, from Figure 10a–c, the range of the optical force component F_y along the y -axis almost keeps the same width, which is different from the magnitude of the numerical value. The beam convergence points along the z -axis are basically at the same position; The beam spread angle distributed along the z -axis (far from the beam convergence point) keeps the same bending degree. On the other hand, when the particle refractive index is greater than the environmental refractive index, the radiation force range, beam convergence point position and beam bending degree (far from the beam convergence point) distributed along the y -axis are all at the same width, the same convergence point position and the same bending degree of the expansion angle from Figure 10d–f. However, only the numerical value of the optical radiation force is different. This is due to the same beam scaling parameter α_0 , beam order l and particle radius when the optical radiation force component F_y is distributed under different particle refractive index.

The distribution of optical force component F_z in Figure 11 resembles that in Figure 10. Nevertheless, in the radiation force distribution F_z of particles with different refractive index below the environmental refractive index, the magnitude of the radiation force component F_z increases with the raising of the particle refractive index. On the contrary, in the F_z distribution of different particle refractive indices (higher than the environmental refractive index), the value of the radiation force component F_z is generally greater than the F_z distribution of different particle refractive indices (lower than the environmental refractive index).

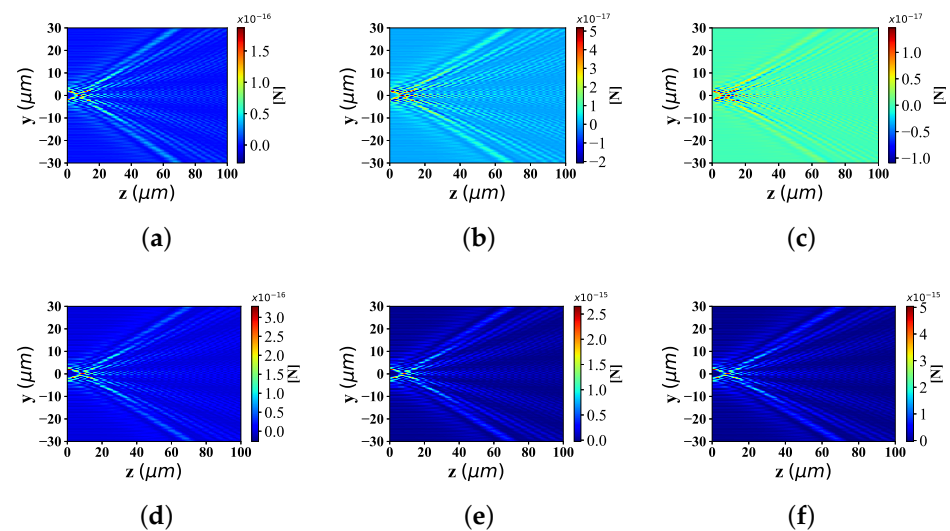


Figure 11. Distribution of F_z under different refractive indices ($m_1 = 1.0, 1.2, 1.3, 1.8, 2.8, 3.8$) for the interaction of Bessel pincer light-sheets beam on the spherical particle. (a) $m_1 = 1.0$; (b) $m_1 = 1.2$; (c) $m_1 = 1.3$; (d) $m_1 = 1.8$; (e) $m_1 = 2.8$; (f) $m_1 = 3.8$.

3.3. F_y and F_z versus the Dimensionless Parameter ka

This subsection describes the variation trend of F_y and F_z with particle radius $radius$ and refractive index m_1 , beam order l and beam scaling parameter α_0 along the propagation direction ($r = \sqrt{y^2 + z^2}$). The incident wave length remains the same as the simulation value in the previous section, and the amplitude of the electromagnetic field remains numerically constant.

Figure 12 shows the distribution of optical force component F_y and F_z with different spherical radius (0.10 μm , 0.12 μm and 0.14 μm , respectively) along the propagation r . When r is equal to 10 μm , the curve gradually tends to converge. Therefore, it is sufficient to discuss the variation of optical force component at a propagation distance of 10 μm . Shown as Figure 12a, at the first stagnation point, F_y with the particle radius of 0.1 μm is zero, F_y with a particle radius of 0.12 μm and F_y with a particle radius of 0.14 μm are also zero. At the first wave crest position, when the particle radius is 0.1 μm , the F_y value is smaller than the F_y value corresponding to the particle radius of 0.12 μm ; The F_y value corresponding to the radius of 0.12 μm is smaller than that corresponding to the particle radius of 0.14 μm . At the second stagnation point, the F_y values corresponding to particle radii of 0.1 μm , 0.12 μm and 0.14 μm are all the same and zero. At the first wave crest, the F_y value corresponding to the particle radius of 0.1 μm is greater than that corresponding to the particle radius of 0.12 μm ; The F_y value corresponding to 0.12 μm radius is greater than that of 0.14 μm particle radius. The position of the third stagnation point is the same as that of the second stagnation point. The F_y values corresponding to different particle radii correspond to zero. At the position of the second wave crest, the distribution of F_y values corresponding to the particle radius is the same as that at the positions of the second wave crest, but the values are smaller. The distribution of F_y value corresponding to particle radius at the second wave trough is the same as that at the first wave trough, but the value is larger. It can be seen that when the distribution of the optical force component F_y changes along the propagation direction, the value of F_y corresponding to different particle radius has positive and negative values. At the same time, it reaches the maximum value at the peak position, the minimum value at the trough position and the zero value at the stagnation point position.

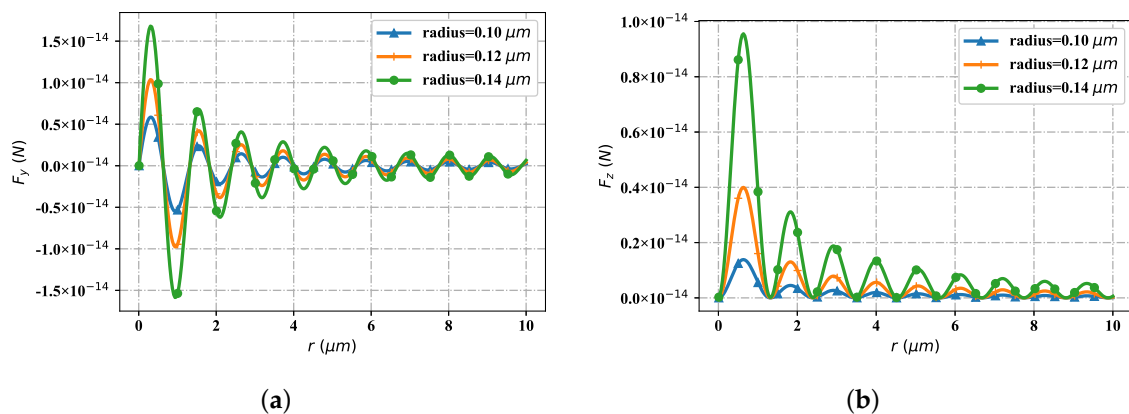


Figure 12. The implication of spherical radius for the changing of F_y and F_z . (a) F_y with radius; (b) F_z with radius.

As shown in Figure 12b, at the first stagnation point, the F_z value corresponding to the radius of all particles is zero. At the first wave crest, the F_z value of particle radius 0.1 μm is smaller than the F_z value corresponding to particle radius 0.12 μm ; When the particle radius is 0.12 μm , the F_z value is smaller than that corresponding to the particle radius of 0.14 μm . The F_z distribution corresponding to the particle radius at the second stagnation point is the same as that at the first location ($F_z = 0$). At the position of the second wave crest, the F_z values corresponding to all particle radii are smaller than those at the position of the first wave crest, but the distribution of the F_z values corresponding to particle radii is similar to that at the first wave crest. The F_z value corresponding to the particle radius at the third, fourth and subsequent stagnation points is zero. The F_z value corresponding to the particle radius at the third and subsequent wave crest gradually decreases, but the distribution is similar to that at the first wave crest. It can be seen that, when the optical force component changes along the direction of propagation, the values of F_z corresponding to the different particle radii are greater than or equal to zero. Moreover, at the same time the maximum value at the peak position is reached, the station position at the same time reaches the value zero- there is no trough. In a word, the F_y component is distributed with the particle radius, showing staggered distribution of wave crest, stagnation point and wave trough. The F_y value at the wave crest is larger with the increase of particle radius, and the overall F_y value decreases gradually with the increase of the number of wave crests; The F_y value at the wave trough is smaller with the increase of particle radius, and the overall F_y value gradually increases with the increase of the number of wave peaks. The F_z component is distributed alternately with the wave crest and the stationary point as the particle radius increases. The F_z value at the wave crest increases as the particle radius increases, and the overall value decreases gradually with the number of wave crests.

Figure 13 shows that the spatial distribution trend of the optical radiation force component F_y with the change of particle refractive index. Ambient refractive index is $m_2 = 1.36$, considering two cases: the particle refractive index is less than the environmental refractive index and the particle refractive index is greater than the environmental refractive index. As shown in Figure 13a (the particle refractive index is smaller than the environmental refractive index), at the first stagnation point, the F_y values of different refractive indexes tend to zero. At the first wave crest position, when the particle refractive index is 1.1, the F_y value is smaller than the F_y value corresponding to the particle refractive index of 1.2; When the particle refractive index is 1.2, the F_y value is smaller than the F_y value corresponding to the particle refractive index of 1.3. At the second stagnation point, the F_y values corresponding to particles with different refractive indexes are all zero. At the first wave trough position, when the particle refractive index is 1.1, the F_y value is greater than the F_y value corresponding to the particle refractive index of 1.2. At the third and all other stagnation points, the F_y values of particles with different refractive index are zero. At the

second wave crest, the distribution of F_y values of different particle refractive indices is similar to that at the first wave crest, but the overall value is smaller than that at the first wave crest. The distribution of F_y value of the particle refractive index at the second wave trough is similar to that of the particle refractive index at the first wave trough, but the overall F_y value is larger. At the third wave crest and the wave crest after it, the distribution of F_y values of different refractive indexes is similar to that at the second wave crest, but the overall value is smaller. At the third and subsequent wave troughs, the distribution of F_y values of different refractive indexes is similar to that at the second wave trough, but the overall value gradually increases. As shown in Figure 13b (the particle refractive index is all greater than the environmental refractive index), the distribution trend of F_y values corresponding to different particle refractive indexes is similar to that in Figure 13a, but the overall value is an order of magnitude higher. With the increase of the refractive index of different particles, the F_y value corresponding to the refractive index of different particles at the wave crest gradually increases, the F_y value corresponding to the refractive index of different particles at the stagnation point is zero, and the F_y value corresponding to the refractive index of different particles at the wave trough gradually decreases.

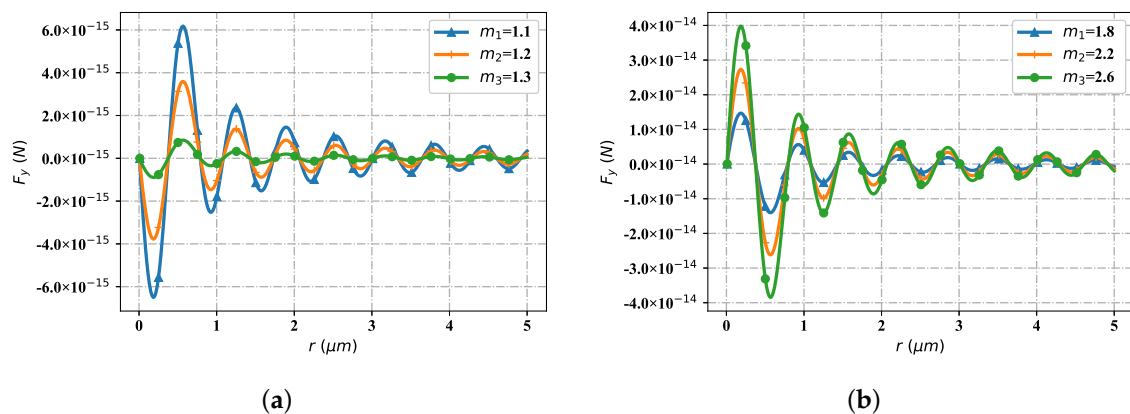


Figure 13. The distribution of F_y under different refractive indices, including the lower indices and upper indices (comparing to the surrounding index). (a) F_y with low indices; (b) F_y with high indices.

Figure 14 contains the change of particle refractive index, but the spatial distribution trend of the optical radiation force component F_z . Similarly, consider two cases: the particle refractive index is less than the environment refractive index and the particle refractive index is greater than the environment refractive index. As shown in Figure 14a (the particle refractive index is smaller than the environmental refractive index), at the first stagnation point, the particle F_z values of different refractive indexes are all zero. At the first wave crest, when the particle refractive index is 1.1, the F_z value is smaller than the corresponding F_z value when the particle refractive index is 1.2; The F_z value when the particle refractive index is 1.2 is smaller than the corresponding F_z value when the particle refractive index is 1.3. All F_z values at the second and subsequent stagnation points tend to zero. At the second wave crest, the distribution trend of F_z values corresponding to particles with different refractive index is similar to that at the first wave crest, but the overall F_z values are smaller than those of particles at the first wave crest. At the third and subsequent wave peaks, the distribution trend of F_z values of particles with different refractive indexes is similar to that at the second wave peak, but the overall values gradually decrease. As shown in Figure 14b (the particle refractive index is greater than the environmental refractive index), the change trend of F_z values corresponding to particles with different refractive index is similar to that in Figure 14a, but the overall F_z value is one order of magnitude higher. At the stagnation point, the F_z values corresponding to different particle refractive indices tend to zero; At the wave crest, the corresponding F_z value gradually increases with the increase of the particle refractive index value; The further it moves back, the smaller the F_z

values corresponding to different particle refractive indices at the wave crest become, but the changing trend remains unchanged.

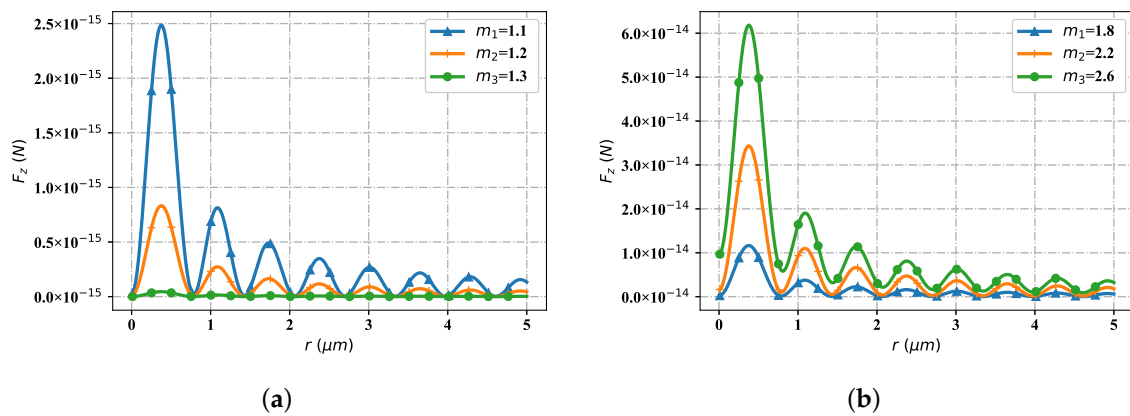


Figure 14. The distribution of F_z under different refractive indices, including the lower indices and upper indices. (a) F_z with low indices; (b) F_z with upper indices.

Figure 15 shows the variation trend of the optical force components F_y and F_z interacting with particles and beams in the space propagation area with different beam parameters (beam order $l = 1$, radius is equal to $0.1 \mu\text{m}$). Through simulation tests, when the spatial position is selected as $r = 6 \mu\text{m}$, the change of optical force component tends to converge under different beam parameters. Figure 15a shows the distribution trend of the optical force component F_y with different beam scaling parameters. At the first stagnation point, for different scale parameters α_0 , the value of F_y tends to zero. When beam scaling parameter $\alpha_0 = 0.6$, the first wave crest appears in the value of F_y ; When beam scaling parameter $\alpha_0 = 0.5$, the value of F_y exhibits a second peak, but the value is smaller than the first peak, and it is farther from the source point of the light source than the first peak; Further, when the beam scaling parameter $\alpha_0 = 0.4$, the value of F_y exhibits a third peak, which is smaller than the second peak, and is farther from the source point of the light source than the second peak. When the value of F_y becomes negative with the beam scaling parameter α_0 , the value of F_y corresponding to $\alpha_0 = 0.6$ first reaches the minimum value of the wave trough; The second is beam scaling parameter α_0 . The value of F_y corresponding to $\alpha_0 = 0.5$ becomes the minimum value of the second wave valley. The value of F_y is larger than that of the first wave valley, and the position is farther from the source point of the light source than that of the first wave valley; When the beam parameter is $\alpha_0 = 0.4$, the corresponding value of F_y becomes the third wave valley, which is larger in value than the corresponding value of F_y at the second wave valley, and is farther from the source point of the light source than the second wave valley. The second group (the fourth, fifth and sixth) wave crest and its subsequent peak digit value and location distribution are similar to those of the first group (the first, second and third), but the overall value becomes smaller. Figure 15b displays the distribution trend of the optical force with different beam scaling parameters, but with respect to the component F_z (all F_z values are greater than or equal to zero). Near the source point of the light source, the value of F_z corresponding to different beam scale parameters tends to zero. When the F_z value corresponding to $\alpha_0 = 0.4$ reaches the first wave peak, the F_z value corresponding to $\alpha_0 = 0.5$ reaches the wave peak, but the F_z value is smaller than the value of $\alpha_0 = 0.4$, and the position of the wave peak is closer to the position of the wave source. When the F_z value corresponding to $\alpha_0 = 0.6$ reaches the first wave peak, the F_z value corresponding to $\alpha_0 = 0.5$ is smaller, but closer to the position of the wave source. For F_z corresponding to $\alpha_0 = 0.4$, $\alpha_0 = 0.5$ and $\alpha_0 = 0.6$, the situation when it reaches the second peak is similar to that when it reaches the first peak, but the overall value is smaller. The F_z value of $\alpha_0 = 0.4$, $\alpha_0 = 0.5$ and $\alpha_0 = 0.6$ respectively reach the third peak, the fourth peak and the subsequent peak, and so on until convergence.

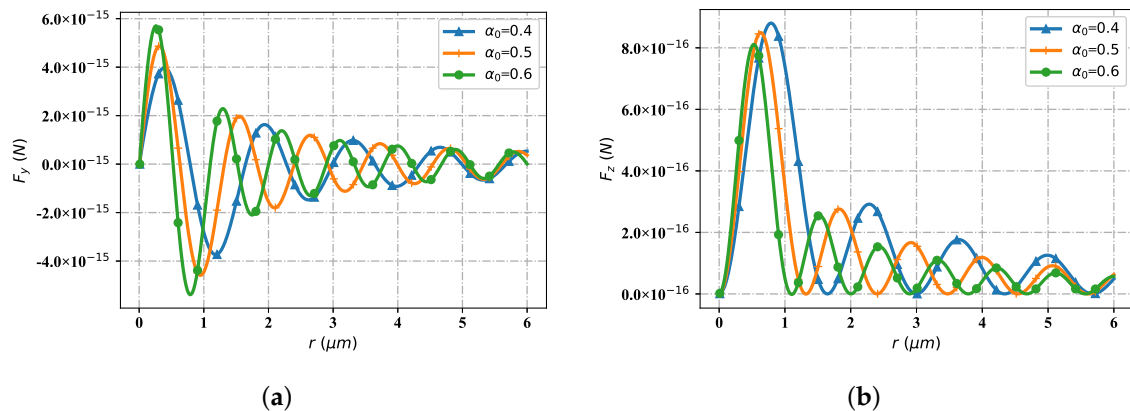


Figure 15. The influence of beam scaling parameter α_0 for optical force component F_y and F_z . (a) F_y with different α_0 ; (b) F_z with different α_0 .

Figure 16 represents the spatial distribution of the optical radiation force component when the Bessel pincer light sheets beam interacts with particles as the beam order changes (particle radius is $0.1 \mu\text{m}$, beam scaling parameter $\alpha_0 = 0.5$, incident wave length is $\lambda = 1.064 \mu\text{m}$, beam order l is 10, 15 and 25). When the spatial position is $r = 25 \mu\text{m}$, the distribution of radiation force component tends to converge. Figure 16a shows the distribution of the radiation force component F_y with the change of spatial position with different beam orders. The wave crest of F_y curve with beam order of $l = 10$ first reaches the first peak near the wave source; The next step is the F_y curve with the beam order of $l = 15$. Relative to the curve with beam order of $l = 10$, the peak position is reached at the second place with a smaller peak but far from the wave source. When the F_y curve with beam order of $l = 10$ and $l = 15$ alternately reaches its corresponding peak, the curve with beam order of $l = 25$ reaches its first peak position (the second peak position of the F_y curve with the relative to beam order of $l = 15$) for the first time. Then, the F_y curves corresponding to the three beam orders interlace with each other in turn and reach the subsequent peak positions respectively. In general, for the F_y curve with beam order $l = 10$, the value of F_y corresponding to the wave crest is higher than that of the F_y curve with beam order $l = 15$, and the value of F_y curve with beam order $l = 25$ is the lowest among the three. On the contrary, in the trough period, the value of F_y curve with beam order of $l = 25$ is the highest among the three, followed by F_y curve with beam order of $l = 15$, and finally by F_y curve with beam order of $l = 10$. Figure 16b shows the radiation force component F_z , which changes with the spatial location distribution under the influence of beam order. With the staggered distribution of wave crests, the F_z components are numerically greater than or equal to zero. When the F_z curve of beam order $l = 10$ first reaches the first wave peak at a position close to the wave source with a large value; The F_z curve with the beam order $l = 15$ reaches the first wave peak with a smaller value at the position far from the wave source. When the F_z curve with the beam order $l = 15$ reaches the third peak, the F_z curve with beam order $l = 25$ starts to reach its first peak (numerically smaller than the first peak of the F_z curve with beam order $l = 15$). Then, the peak value of each order successively reaches the corresponding peak until convergence.

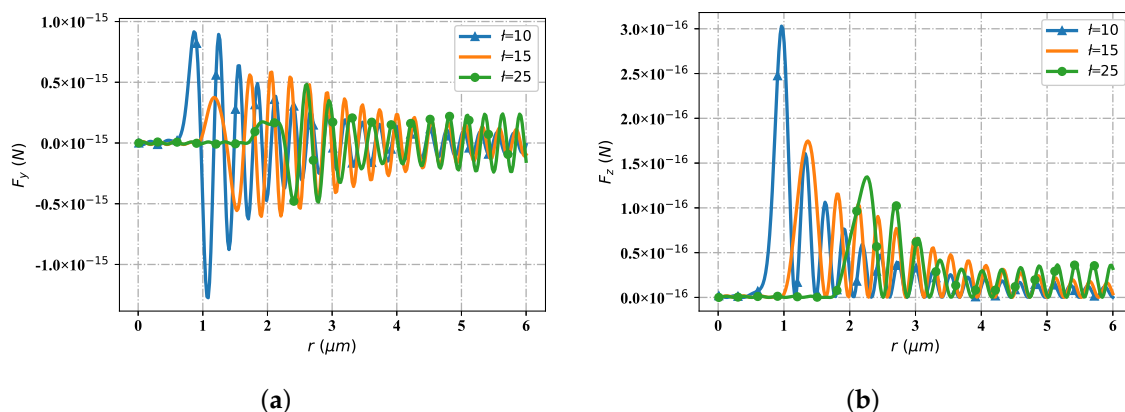


Figure 16. The influence of beam order l for optical force component F_y and F_z . (a) F_y with different l ; (b) F_z with different l .

4. Conclusions

The result reported above was obtained by using GLMT which is based on the Maxwell stress tensor method, and electromagnetic field expression. We discussed two aspects: one is the influence of spherical particle parameters, the other is the implication of Bessel Pincer light-sheets beam parameters. By showing the results of the pseudo-color map and comparing the results of the line graph, we acknowledge that the change of particle parameters affects the magnitude of the corresponding numerical value of the radiation force component. Furthermore, the change of beam parameters affects the distance of radiation force convergence position (from the wave source), and the degree of beam divergence and bending (after the distance from the wave source position). According to the control variable method, for the particle parameters, the value of the radiation force increases with the growing of the particle refractive index and the equivalent radius. As for beam parameters, with the improving of beam order l , the distribution range of radiation force along the y -axis gradually expands, the beam convergence location is farther and farther away from the wave source, and the bending degree away from the wave source convergence location gradually presents a small angle; On the contrary, with the amplifying of beam scale parameters α_0 , the distribution range of radiation force along the y -axis gradually narrows, the beam convergence location is closer to the wave source location, and the bending degree away from the wave source convergence location gradually presents a larger angle. The result presented here opens a new landscape of possible phenomena for anatomy of biological cells in two dimensions, including particle rotating and sorting devices, optical sectioning, imaging microscopy and particle characterization and sizing.

Author Contributions: Conceptualization, R.L.; Data curation, N.S.; Funding acquisition, B.W., Q.W. and R.L.; Supervision, B.W., Q.W., R.L. and S.C.; Visualization, S.Z.; Writing—original draft, S.Z.; Writing—review and editing, B.W., Q.W., R.L. and S.C. All authors have read and agreed to the published version of the manuscript.

Funding: This work was supported by the Graduate Innovation Foundation of Xidian University (YJS2208); The National Natural Science Foundation of China [61901324, 62001345, 62201411]. The China Postdoctoral Science foundation [2019M653548, 2019M663928XB]; the Fundamental Research Funds for the Central Universities (XJS200501, XJS200507, JB200501, XJS222704, QTZX22021).

Data Availability Statement: Some or all data, models, or code generated or used during the study are available in a repository or online in accordance with funder data retention policies (Provide full citations that include URLs or DOIs.)

Conflicts of Interest: The authors declare no conflict of interest.

Abbreviations

The following abbreviations are used in this manuscript:

GLMT Genralized Lorenz Mie Theory

References

1. Dholakia, K.; Reece, P. Optical micromanipulation takes hold. *Nano Today* **2006**, *1*, 18–27. [[CrossRef](#)]
2. Chen, J.; Ng, J.; Lin, Z.; Chan, C.T. Optical pulling force. *Nat. Photonics* **2011**, *5*, 531–534. [[CrossRef](#)]
3. Karásek, V.; Čížmár, T.; Brzobohatý, O.; Zemánek, P.; Garcés-Chávez, V.; Dholakia, K. Long-range one-dimensional longitudinal optical binding. *Phys. Rev. Lett.* **2008**, *101*, 143601. [[CrossRef](#)]
4. Yamanishi, J.; Yamane, H.; Naitoh, Y.; Li, Y.J.; Yokoshi, N.; Kameyama, T.; Sugawara, Y. Optical force mapping at the single-nanometre scale. *Nat. Commun.* **2021**, *12*, 3865. [[CrossRef](#)] [[PubMed](#)]
5. Huang, C.H.; Louis, B.; Bresolí-Obach, R.; Kudo, T.; Camacho, R.; Scheblykin, I.G.; Masuhara, H. The primeval optical evolving matter by optical binding inside and outside the photon beam. *Nat. Commun.* **2022**, *13*, 5325. [[CrossRef](#)]
6. Zhong, M.C.; Wei, X.B.; Zhou, J.H.; Wang, Z.Q.; Li, Y.M. Trapping red blood cells in living animals using optical tweezers. *Nat. Commun.* **2013**, *4*, 1768. [[CrossRef](#)]
7. Ge, J.; Bian, X.; Ma, L.; Cai, Y.; Li, Y.; Yang, J.; Zhang, Y. Stepwise membrane binding of extended synaptotagmins revealed by optical tweezers. *Nat. Chem. Biol.* **2022**, *18*, 313–320. [[CrossRef](#)] [[PubMed](#)]
8. Pochitaloff, M.; Miranda, M.; Richard, M.; Chaiyasitdhi, A.; Takagi, Y.; Cao, W.; Martin, P. Flagella-like beating of actin bundles driven by self-organized myosin waves. *Nat. Phys.* **2022**, *18*, 1240–1247. [[CrossRef](#)]
9. Das, S.; Butenko, A.V.; Mastai, Y.; Deutsch, M.; Sloutskin, E. Topology-driven surface patterning of liquid spheres. *Nat. Phys.* **2022**, *18*, 1177–1180. [[CrossRef](#)]
10. Swartzlander, G.A.; Peterson, T.J.; Artusio-Glimpse, A.B.; Raisanen, A.D. Stable optical lift. *Nat. Photonics* **2011**, *5*, 48–51. [[CrossRef](#)]
11. Simpson, S.H.; Hanna, S.; Peterson, T.J.; Swartzlander, G.A. Optical lift from dielectric semicylinders. *Opt. Lett.* **2012**, *37*, 4038–4040. [[CrossRef](#)] [[PubMed](#)]
12. Rosenberg, J.; Lin, Q.; Painter, O. Static and dynamic wavelength routing via the gradient optical force. *Nat. Photonics* **2009**, *3*, 478–483. [[CrossRef](#)]
13. Liang, H.; Wright, W.H.; Cheng, S.; He, W.; Berns, M.W. Micromanipulation of chromosomes in PTK2 cells using laser microsurgery (optical scalpel) in combination with laser-induced optical force (optical tweezers). *Exp. Cell Res.* **1993**, *204*, 110–120. [[CrossRef](#)] [[PubMed](#)]
14. Bayles, C.J.; Aist, J.R.; Berns, M.W. The mechanics of anaphase B in a basidiomycete as revealed by laser microbeam microsurgery. *Exp. Mycol.* **1993**, *17*, 191–199. [[CrossRef](#)]
15. Fuhr, G.; Reichle, C.; Müller, T.; Kahlke, K.; Schütze, K.; Stuke, M. Processing of micro-particles by UV laser irradiation in a field cage. *Appl. Phys. A* **1999**, *69*, 611–616. [[CrossRef](#)]
16. Jarvis, J.; Lebedev, V.; Romanov, A.; Broemmelsiek, D.; Carlson, K.; Chattopadhyay, S.; Valishev, A. Experimental demonstration of optical stochastic cooling. *Nature* **2022**, *608*, 287–292. [[CrossRef](#)]
17. Peschel, M.T.; Högner, M.; Buberl, T.; Keefer, D.; de Vivie-Riedle, R.; Pupeza, I. Sub-optical-cycle light-matter energy transfer in molecular vibrational spectroscopy. *Nat. Commun.* **2022**, *13*, 5897. [[CrossRef](#)] [[PubMed](#)]
18. Yin, P.; Li, R.; Yin, C.; Xu, X.; Bian, X.; Xie, H.; Du, J. Experiments with levitated force sensor challenge theories of dark energy. *Nat. Phys.* **2022**, *18*, 1181–1185. [[CrossRef](#)]
19. Peddireddy, K.R.; Clairmont, R.; Neill, P.; McGorty, R.; Robertson-Anderson, R.M. Optical-Tweezers-integrating-Differential-Dynamic-Microscopy maps the spatiotemporal propagation of nonlinear strains in polymer blends and composites. *Nat. Commun.* **2022**, *13*, 5180. [[CrossRef](#)]
20. Chaudhuri, O.; Parekh, S.H.; Lam, W.A.; Fletcher, D.A. Combined atomic force microscopy and side-view optical imaging for mechanical studies of cells. *Nat. Methods.* **2009**, *6*, 383–387. [[CrossRef](#)]
21. Phillips, D.B.; Padgett, M.J.; Hanna, S.; Ho, Y.L.D.; Carberry, D.M.; Miles, M.J.; Simpson, S.H. Shape-induced force fields in optical trapping. *Photonics* **2014**, *8*, 400–405. [[CrossRef](#)]
22. Lebedew, P. Untersuchungen über die Druckkräfte des Lichtes. *Ann. Phys.* **1901**, *311*, 433–458. [[CrossRef](#)]
23. Lebedev, P.N. LEBEDEV 1901. *Ann. Phys.* **1901**, *6*, 433.
24. Hull, G.F.; Bell, M.; Green, S.E. Notes on the Pressure of Radiation. *Proc. Phys. Soc.* **1934**, *46*, 589. [[CrossRef](#)]
25. Ashkin, A. Acceleration and trapping of particles by radiation pressure. *Phys. Rev. Lett.* **1970**, *24*, 156. [[CrossRef](#)]
26. Ashkin, A.; Dziedzic, J.; Yamane, T. Optical trapping and manipulation of single cells using infrared laser beams. *Nature* **1987**, *330*, 769–771. [[CrossRef](#)]
27. Gordon, J.P. Radiation forces and momenta in dielectric media. *Phys. Rev. A* **1973**, *8*, 14. [[CrossRef](#)]
28. Purcell, E.M.; Pennypacker, C.R. Scattering and absorption of light by nonspherical dielectric grains. *Astrophys. J.* **1973**, *186*, 705–714. [[CrossRef](#)]
29. Volpe, G.; Helden, L.; Brettschneider, T.; Wehr, J.; Bechinger, C. Influence of noise on force measurements. *Phys. Rev. Lett.* **2010**, *104*, 2010. [[CrossRef](#)]

30. Yurkin, M.A.; Hoekstra, A.G. The discrete-dipole-approximation code ADDA: Capabilities and known limitations. *J. Quant. Spectrosc. Radiat. Transfer.* **2011**, *112*, 2234–2247. [[CrossRef](#)]
31. Wei, B.; Li, R.; Zhang, S.; Zhang, J.; Xu, Q.; Song, N.; Sun, H. Photonic jet generated by a dielectric ellipsoidal particle. *J. Quant. Spectrosc. Radiat. Transfer.* **2020**, *242*, 106786. [[CrossRef](#)]
32. Zhang, S.; Li, R. In Proceedings of the 2019 IEEE International Conference on Computational Electromagnetics (ICCEM), Shanghai, China, 20–22 March 2019.
33. Mie, G. Beiträge zur Optik trüber Medien, speziell kolloidaler Metallösungen. *Ann. Phys.* **1908**, *330*, 377–445. [[CrossRef](#)]
34. Casperson, L.W.; Yeh, C. Rayleigh-Debye scattering with focused laser beams. *Ann. Phys.* **1978**, *17*, 1637–1643. [[CrossRef](#)] [[PubMed](#)]
35. Kim, J.S.; Lee, S.S. Scattering of laser beams and the optical potential well for a homogeneous sphere. *J. Opt. Soc. Am.* **1983**, *73*, 303–312. [[CrossRef](#)]
36. Gouesbet, G.; Maheu, B.; Gréhan, G. Light scattering from a sphere arbitrarily located in a Gaussian beam, using a Bromwich formulation. *J. Opt. Soc. Am.* **1988**, *5*, 1427–1443. [[CrossRef](#)]
37. Barton, J.P.; Alexander, D.R.; Schaub, S.A. Internal and near-surface electromagnetic fields for a spherical particle irradiated by a focused laser beam. *J. Appl. Phys.* **1988**, *64*, 1632–1639. [[CrossRef](#)]
38. Barton, J.P.; Alexander, D.R.; Schaub, S.A. Theoretical determination of net radiation force and torque for a spherical particle illuminated by a focused laser beam. *J. Appl. Phys.* **1989**, *66*, 4594–4602. [[CrossRef](#)]
39. Brevik, I. Experiments in phenomenological electrodynamics and the electromagnetic energy-momentum tensor. *J. Phys. Rep.* **1979**, *52*, 133–201. [[CrossRef](#)]
40. Scott, W.T. Electromagnetism (Oxford Physics Series) by FNH Robinson. *Reviewer* **1976**, 611–616.
41. Mitri, F.G. Radiation force and torque of light-sheets. *J. Opt.* **2017**, *19*, 065403. [[CrossRef](#)]
42. Li, R.; Shi, L.; Ren, K. F.; Jiang, H. Debye series for Gaussian beam scattering by a multilayered sphere. *Appl. Opt.* **2007**, *46*, 4804–4812. [[CrossRef](#)] [[PubMed](#)]
43. Gašparić, V.; Mayerhöfer, T. G.; Zopf, D.; Ristić, D.; Popp, J.; Ivanda, M. To generate a photonic nanojet outside a high refractive index microsphere illuminated by a Gaussian beam. *Opt. Lett.* **2022**, *47*, 2534–2537. [[CrossRef](#)] [[PubMed](#)]
44. Yang, R.; Li, R. Optical force exerted on a Rayleigh particle by a vector arbitrary-order Bessel beam. *J. Quant. Spectrosc. Radiat. Transfer.* **2016**, *178*, 230–243. [[CrossRef](#)]
45. Li, X.; Chen, J.; Lin, Z.; Ng, J. Optical pulling at macroscopic distances. *Sci. Adv.* **2019**, *5*, eaau7814. [[CrossRef](#)] [[PubMed](#)]
46. Fan, X.D.; Zhang, L. Trapping force of acoustical Bessel beams on a sphere and stable tractor beams. *Phys. Rev. Appl.* **2019**, *11*, 014055. [[CrossRef](#)]
47. Berry, M.V.; Balazs, N.L. Nonspreading wave packets. *Am. J. Phys.* **1979**, *47*, 264–267. [[CrossRef](#)]
48. Zhang, S.; Li, R.; Wei, B.; Zhang, J.; Sun, H.; Song, N. Scattering of a non-paraxial Bessel light-sheet by a sphere of arbitrary size. *Opt. Express.* **2020**, *245*, 106869. [[CrossRef](#)]
49. Durnin, J.; Miceli, J.J., Jr.; Eberly, J.H. Diffraction-free beams. *Phys. Rev. Lett.* **1987**, *58*, 1499. [[CrossRef](#)]
50. Zhao, Z.; Zang, W.; Tian, J. Optical trapping and manipulation of Mie particles with Airy beam. *J. Opt.* **2016**, *18*, 025607. [[CrossRef](#)]
51. Baumgartl, J.; Mazilu, M.; Dholakia, K. Optically mediated particle clearing using Airy wavepackets. *Nat. Photonics* **2008**, *2*, 675–678. [[CrossRef](#)]
52. Wang, M.M.; Tu, E.; Raymond, D.E.; Yang, J.M.; Zhang, H.; Hagen, N.; Dees, B.; Mercer, E.M.; Forster, A.H.; Kariv, I.; et al. Microfluidic sorting of mammalian cells by optical force switching. *Nat. Biotechnol.* **2005**, *23*, 83–87. [[CrossRef](#)] [[PubMed](#)]
53. Brau, R.R.; Tarsa, P.B.; Ferrer, J.M.; Lee, P.; Lang, M.J. Interlaced optical force-fluorescence measurements for single molecule biophysics. *Biophys. J.* **2006**, *91*, 1069–1077. [[CrossRef](#)] [[PubMed](#)]
54. Choi, B.; Jia, W.; Channual, J.; Kelly, K.M.; Lotfi, J. The importance of long-term monitoring to evaluate the microvascular response to light-based therapies. *J. Investig. Dermatol.* **2008**, *128*, 485. [[CrossRef](#)] [[PubMed](#)]
55. Otte, E.; Denz, C. Optical trapping gets structure: Structured light for advanced optical manipulation. *Appl. Phys. Rev.* **2020**, *7*, 041308. [[CrossRef](#)]
56. Mitri, F.G. Circularly-polarized Airy light-sheet spinner tweezers and particle transport. *J. Quant. Spectrosc. Radiat. Transfer.* **2021**, *260*, 107466. [[CrossRef](#)]
57. Mitri, F.G. Negative optical radiation force and spin torques on subwavelength prolate and oblate spheroids in fractional Bessel–Gauss pincers light-sheets. *J. Opt. Soc. Am. A* **2017**, *34*, 1246–1254. [[CrossRef](#)]
58. Mitri, F.G. Unconventional circularly polarized Airy light-sheet spinner tweezers. *J. Opt. Soc. Am. A* **2021**, *38*, 526–533. [[CrossRef](#)]
59. Zhang, S.; Li, R.; Wei, B.; Song, N.; Yang, L.; Sun, H. Scattering of a non-paraxial Bessel pincer light-sheet by a dielectric sphere of arbitrary size. *J. Quant. Spectrosc. Radiat. Transfer.* **2021**, *268*, 107647. [[CrossRef](#)]
60. Mitri, F.G. Nonparaxial Bessel and Bessel–Gauss pincers light-sheets. *Phys. Lett. A* **2017**, *381*, 171–175. [[CrossRef](#)]
61. Lu, W.; Chen, H.; Liu, S.; Lin, Z. Rigorous full-wave calculation of optical forces on dielectric and metallic microparticles immersed in a vector Airy beam. *Opt. Express.* **2017**, *25*, 23238–23253. [[CrossRef](#)]
62. Trukhanov, S.V.; Trukhanov, A.V.; Turchenko, V.A.; Trukhanov, A.V.; Trukhanova, E.L.; Tishkevich, D.; Ivanov, V.M.; Zubar, T.I.; Salem, M.; Kostishyn, V.G.; et al. Polarization origin and iron positions in indium doped barium hexaferrites. *Ceram. Int.* **2018**, *44*, 290–300. [[CrossRef](#)]

63. Kozlovskiy, A.; Kenzhina, I.; Alyamova, Z.A.; Zdorovets, M. Optical and structural properties of AlN ceramics irradiated with heavy ions. *Opt. Mater.* **2019**, *91*, 130–137. [[CrossRef](#)]
64. Kozlovskiy, A.L.; Zdorovets, M.V. Effect of doping of $Ce^{4+/3+}$ on optical, strength and shielding properties of $(0.5-x) TeO_2-0.25 MoO-0.25 Bi_2O_3-xCeO_2$ glasses. *Mater. Chem. Phys.* **2021**, *263*, 124444. [[CrossRef](#)]
65. Turchenko, V.A.; Trukhanov, S.V.; Kostishin, V.G.E.; Damay, F.; Porcher, F.; Klygach, D.S.; Vakhitov, M.G.; Matzui, L.Y.; Yakovenko, O.S.; Bozzo, B.; et al. Impact of In^{3+} cations on structure and electromagnetic state of M-type hexaferrites. *J. Energy Chem.* **2022**, *69*, 667–676. [[CrossRef](#)]
66. Kozlovskiy, A.L.; Zdorovets, M.V. Synthesis, structural, strength and corrosion properties of thin films of the type CuX (X= Bi, Mg, Ni). *J. Mater. Sci. Mater. Electron.* **2019**, *30*, 11819–11832. [[CrossRef](#)]
67. Zubar, T.I.; Fedosyuk, V.M.; Trukhanov, S.V.; Tishkevich, D.I.; Michels, D.; Lyakhov, D.; Trukhanov, A.V. Method of surface energy investigation by lateral AFM: application to control growth mechanism of nanostructured NiFe films. *Sci. Rep.* **2020**, *10*, 14411. [[CrossRef](#)]
68. Chaumet, P.C.; Rahmani, A. Electromagnetic force and torque on magnetic and negative-index scatterers. *Opt. Express.* **2009**, *17*, 2224–2234. [[CrossRef](#)]